# Stability of sandy soils against internal erosion under cyclic loading and quantitatively examination of the composition and origin of eroded particles

Shaoheng Dai[1]; Xuzhen He[2]; Chenxi Tong[3]; Feng Gao[4]; Sheng Zhang[5]; and Daichao Sheng[6]

**Shaoheng Dai**, Ph.D. student

1. School of Civil Engineering, Central South University, Changsha, Hunan 410075, China.

2. School of Civil and Environmental Engineering, University of Technology Sydney, Ultimo, NSW 2007, Australia.

Email: shaoheng.dai@student.uts.edu.au

**Xuzhen He**, Senior Lecturer

School of Civil and Environmental Engineering, University of Technology Sydney, Ultimo, NSW 2007, Australia.

Email: xuzhen.he@uts.edu.au

**Chenxi Tong**, Associate Professor

School of Civil Engineering, Central South University, Changsha, 410075, China.

Email: cxtong@csu.edu.cn

**Feng Gao**, Postdoctoral Fellow

National Engineering Research Center of Highway Maintenance Technology, School of Traffic and Transportation Engineering, Changsha University of Science & Technology, Changsha, 410114, Hunan, China

Email: gao-feng@csust.edu.cn

**Sheng Zhang**, Professor

**(Corresponding author)**

1. School of Civil Engineering, Central South University, Changsha, 410075, China.
2. School of Civil Engineering, Qinghai University, Xining, 810016, China

Email: zhang-sheng@csu.edu.cn

**Daichao Sheng**, Distinguished Professor

School of Civil and Environmental Engineering, University of Technology Sydney, Ultimo, NSW 2007, Australia.

Email: Daichao.Sheng@uts.edu.au

**ABSTRACT**: Internal erosion refers to the movement of fine particles within soil framework due to subsurface water seepage. Existing criteria for assessing internal erosion usually are based on static loading and the effect of cyclic load is not considered. Additionally, there are limited studies to examine the particle-size distribution and origin of eroded fine particles. This work presents an experimental investigation that examines the impact of cyclic loading on internal stability through a series of seepage tests. The composition and origin of lost particles are quantitatively studied using particle staining and image recognition techniques. With increasing hydraulic gradient, particle erosion progresses from top layer to bottom layer, with a gradual increase in the maximum particle size of eroded particles from each layer. After significant loss of particles, the specimens reach a state of transient equilibrium, resulting in a gradual slowdown of both particle loss rate and average flow velocity. The results indicate that cyclic loading promotes massive particle loss and causes erosion failure of specimens that are considered stable according to existing criteria. The reason is that under cyclic loading, local hydraulic gradients is oscillating, and a larger than average hydraulic gradient may occur, which is responsible for the internal instability. The analysis suggests that existing criteria can provide a reasonable assessment of the relative stabilities of specimens under static loads, but fail to capture the stabilities under cyclic loading conditions.

**Keywords**: Internal erosion; Internal stability; Cyclic loading; Dyeing particles; Hydraulic gradient; Porosity

## 1. Introduction

Internal erosion stands as a prominent factor contributing to the failure of various hydraulic structures such as embankments and dams (Bonelli et al. 2006; Chang and Zhang, 2013; Foster et al. 2000; Jin et al. 2022; Liang et al. 2017; Richards and Reddy 2007; Wang et al. 2022). The fundamental mechanisms underlying internal erosion primarily encompass leak erosion, backward erosion, suffusion, and contact erosion (Fleshman and Rice 2014; Hunter and Bowman 2018; Ma et al. 2021; Scheuermann et al. 2002; Sufian et al. 2022; Suits et al. 2011). These different mechanisms have been reported to be the primary reason for the failure of nearly half of the world's levees and dams. As an illustration, the Noto Peninsula Earthquake that occurred in Japan in 2007 resulted in erosion-related damages to road infrastructure, specifically in around 80 locations along the high embankment of the mountainside road (Ke and Takahashi 2014b). In addition, internal erosion can also trigger slope damage and lead to frequent disasters such as landslides and debris flows. As noted by Crosta and Prisco (1999), a slope failure transpired on an old fluvial terrace in Italy. With numerical analysis and site investigation, the authors presented the evolution of seepage and erosion phenomenon. Wide-graded cohesionless soils, such as gravel or silt, are more vulnerable to internal erosion due to their lack of specific grain size (Maknoon and Mahdi 2010). Once internal erosion occurs, the microstructure of soils will change accordingly, resulting in alterations in its physical and geo-mechanical properties (e.g., permeability, particle size distribution, volume change) (Che et al. 2021; Tran et al. 2022; Wautier et al. 2019; Xiao and Shwiyhat 2012; Yan et al. 2022; Zhang et al. 2023).

Extensive experimental tests have been performed primarily to understand internal erosion phenomena (Fell et al. 2003; Flores-Berrones et al. 2011). These studies have primarily focused on soils with varying particle size distributions (PSDs) to extensively examine the effects of

PSDs on internal stability, which refers to the ability to resist the loss of fine particles during seepage flow. Previous studies (Indraratna et al. 2011; Moraci et al. 2014) have put forth the notion that stability is primarily influenced by the shape of PSD curve, facilitating the development of various geometrical criteria. Kenney and Lau (1985) introduced a criterion that evaluates soil stability by examining the impact of PSD on the loss of fine particles. Istomina (1957) proposed an internal stability criterion that employed the uniformity coefficient as a variable. Mao (2005) recommended a method to discriminate between piping soil and non-piping soil through a combination of experimental testing and theoretical deduction. Indraratna et al. (2015) conducted a comprehensive analysis by comparing a significant amount of data to assess the influence of various uniformity coefficients and relative density on soil stability. Based on their findings, they proposed a novel approach called the combined particle and constriction size distribution (CP-CSD) method to evaluate the stability of soils.

Although considerable research has been devoted to internal stability criteria based on geometric conditions, less attention is paid to the influence of complex external mechanical conditions. Most of the studies mentioned above are based on experiments and analysis under steady-state seepage flow, which is critical for understanding internal erosion under static/quasi-static loading. However, the influence of dynamic loads (e.g., cyclic loads, impact loads, etc.) has not been adequately explored. In fact, external dynamic loads are often present during the construction and operation of various types of infrastructure, including dams, railroads, municipal engineering, and other projects. One common example of such loads is vehicle movements, which tends to be long-lasting and repeated. This poses substantial challenges to the internal stability of the soil. To date, numerous researchers have undertaken comprehensive investigations into the impact of cyclic loading on internal erosion, primarily focusing on the evolution of key parameters such as permeability, porosity, and pore water

pressure. Johnston et al. (2021) conducted a thorough review of the causes and types of damage inflicted upon transportation embankments during floods. They expressed concerns regarding the detrimental effects of dynamic conditions, particularly during floods, on the structural stability of these embankments. Israr and Indraratna (2018) examined the mechanical response of granular filters when subjected to cyclic loading, with a specific emphasis on studying the evolving hydraulic parameters throughout the erosion process. Jiang et al. (2015) delved into the evolution of pore water pressure and stress distribution in roadbed soil by constructing a comprehensive full-scale ballastless railway physical mode. Sufian et al. (2022) utilized spatial time domain reflectometry to quantitatively measure the transient evolution of porosity distribution during the internal erosion process. In summary, the growth in transportation demands has led to larger-scale applications of dynamic loading, presenting substantial challenges to the reliability of soil structures. Therefore, it is imperative to undertake comprehensive investigations into soil's internal erosion patterns and its stability when subjected to cyclic loading.

Recent research efforts have been directed towards enhancing our comprehension of the underlying mechanisms of internal erosion, with the aid of new test apparatus and numerical models (David Suits et al. 2006; Gollin et al. 2017; He et al. 2020; Ke and Takahashi 2014a; Lian et al. 2021; Ma et al. 2022; Moffat et al. 2011; Suits et al. 2011). For example, Ke and Takahashi (2014b) investigated the fine particle loss patterns and PSD variations of saturated cohesionless soils under different stress states by conducting percolation tests. Yang et al. (2019) and Yin et al. (2020) established a four-constituent continuum model utilizing the porous continuum medium theory to investigate particle migration during internal erosion. Shire and O'Sullivan (2013) applied the discrete element method to provide a micromechanical explanation for internal erosion and visualize the loss of fine particles. Researchers widely

agree that fine particle loss poses a huge potential risk to structural safety. Although extensive research has been conducted to explore the pattern of fine particle loss, few laboratory tests have been able to account for the specific compositional origin, particle size distribution characteristics, and other details of the eroded soil particles.

The main aims of this study are (1) to evaluate the effect of cyclic loading on internal erosion of sandy soils and (2) to provide a quantitative description of the particle size distribution and compositional origin of the lost particles. In this paper, the key components of the test apparatus and the step-by-step testing procedures are presented in Section 2. In Section 3, the effects of cyclic loading on the stability of sandy soils and the quantitative description of the lost particles are demonstrated. The causes of significant particle loss and premature erosion failure of specimens under cyclic loading are discussed in Section 4.

## 2. Methods and materials

### *2.1 Upward seepage test apparatus*

The internal erosion experiments under upward flow conditions were conducted using an in-house apparatus. The overall configuration of the apparatus is illustrated in Fig. 1. It comprises a water supply system, a loading system, a data acquisition system, and a collection system (soil and water are collected separately). The seepage cell used in the experiments has a cylindrical shape with an internal diameter of 170 mm. The axial loading system applies static or cyclic loading on the top of specimen. An acceleration sensor and a weight sensor are installed to measure load frequency and load magnitude. The data acquisition system includes pore water pressure sensors, Ec-5 humidity sensors, a data acquisition instrument, and a computer. Three pressure transducers (namely P-1, P-2, and P-3) are strategically positioned on the wall of the cylindrical container at depths of 80 mm, 160 mm, and 240 mm, respectively.

Prior to the preparation of the specimen, the installed pressure transducers are immersed in the de-aired water for 24 hours. The EC-5 humidity sensors, measuring 5 cm in length with a measurement volume of 240 $cm^3$, and featuring a range from 0% to 100% with an accuracy of ±2%, have gained extensive use in the monitoring of soil volumetric water content (VWC) (Trautz et al. 2015; Wicki et al. 2020; Tian et al. 2020). The outlet is exposed to the atmosphere, and the inlet is connected to a water head tank that maintains a constant hydraulic head. This setup allows for the adjustment of the hydraulic head to initiate seepage flow and trigger internal erosion. During the experimental process, water flows in an upward direction through the specimen and subsequently spills freely from the top. To capture and collect the eroded particles, a specialized collection system has been devised. This system consists of a funnel, a filter, and a beaker. The eroded particles are carried by water out of the specimen to the collection device during the test. The inclusion of a filter serves the essential purpose of expediting the settling of eroded particles within the funnel, effectively segregating water from the soil. The filter's dimensions are established based on the smallest particle size present in the test soil. Both the funnel and filter are thoughtfully designed for easy disassembly, enabling periodic replacement to gather eroded particles. The mass of the eroded particles is subsequently determined by weighing the collected samples on a lightweight tray. After passing through the funnel and filter, water accumulates in the lower beaker container. To monitor seepage velocity, the increase in collected water within the container is meticulously weighed at specific time intervals using an electronic balance. The detail of each component is reported in Zhang et al. (2021) and Gao et al. (2022).

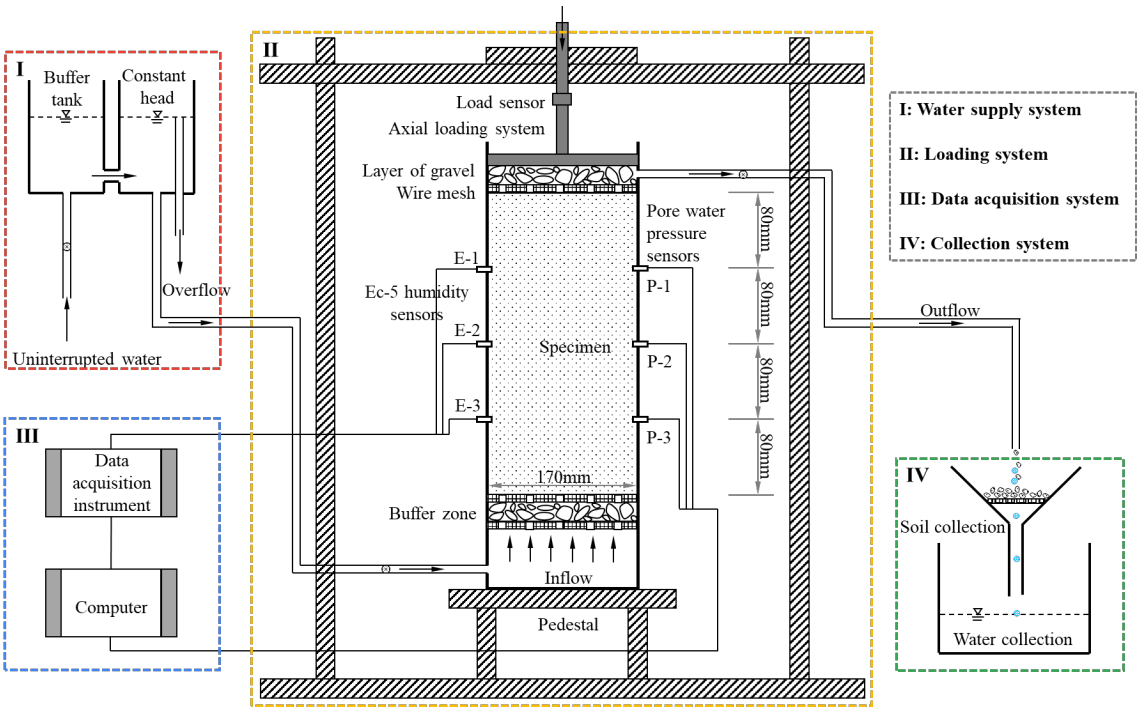


Fig.1. Schematic diagram of the testing apparatus

### *2.2 Materials*

The materials tested in this study are sands that underwent a cleaning process to remove any dirt and impurities prior to conducting the test. Two types of sand were used in the experiment. Their PSDs were measured according to the sieving method recommended by ASTM standard (ASTM, 2014) and results are shown in Fig. 2. Table 1 presents the physical properties of the sands utilized in the study. During the cyclic test, a sinusoidal stress was applied to the top boundary with the following parameters: the mean stress = 35.5 kPa, amplitude = 7 kPa, and load frequency = 8 Hz. The applied loading magnitude in the experiments is representative of the dynamic stress induced by the CRH-380A high-speed train operating on the Wuhan-Guangzhou railway. This stress level corresponds to a standard bogie distance of 2.5 m and an axle load of 15 t, with the train running at an approximate speed of 250 km/h (Qu et al. 2012). In addition to the dynamic loading, a static hydraulic test was conducted where the specimen was subjected to a constant stress of 35.5 kPa. This controlled test was performed to specifically investigate the impact of cyclic loading on internal erosion.

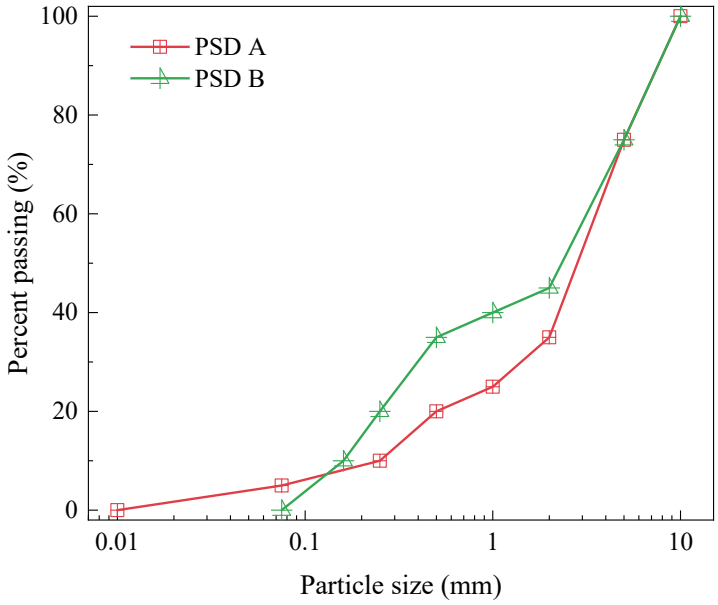


Fig.2. Grain size distribution of materials.

Table 1. Basic physical properties of sands.

| Test identifier | Loading | PSD | Maximum dry density $\rho_{dmax}$/(g/cm$^3$) | Minimum dry density $\rho_{dmin}$/(g/cm$^3$) | Effective size $d_{10}$ /mm | Coefficient of curvature ($C_c$) | Coefficient of uniformity ($C_u$) |
|---|---|---|---|---|---|---|---|
| A-static | static | A | 1.979 | 1.658 | 0.25 | 2.32 | 15.50 |
| A-cyclic | cyclic | A | | | | | |
| B-cyclic | cyclic | B | 2.106 | 1.698 | 0.16 | 0.31 | 21.88 |

The internal stability of the two soils is evaluated using five existing methods proposed by US Army Crops Engineering Engineers (1953), Kenney and Lau (1985, 1986), Kezdi (1979), Istomina (1957), and Burenkova (1993). The assessment details are presented in Table 2, revealing that, overall, Specimen with PSD A is potentially stable for suffusion, while Specimen with PSD B is potentially unstable and vulnerable to internal erosion if seepage takes place.

Table 2. Assessment of internal stability.

| Methods used for assessing internal stability | | Internal stability | |
|---|---|---|---|
| References | The mixture exhibits internal stability when | PSD A | PSD B |
| US Army Crops of Engineers (1953) | $C_u < 20$ | S | U |
| Kenney and Lau (1985, 1986) | $(H/F)_{min} \geq 1$ $(0 < F < 0.2)$ | U | U |
| Kezdi (1979) | $D_{15c}/d_{85f} \leq 4$ | S | U |
| Istomina (1957) | $C_u \leq 20$ | S | U |
| Burenkova (1993) | $0.76\log_{10}(h_2)+1 < h_1 < 1.86\log_{10}(h_2)+1$ | S | S |

Note: $C_u$= coefficient of uniformity; $F$= the weight fraction of the soil particles that are finer than the specified size $d$; $H$= the weight fraction of the soil particles that fall within the size range from $d$ to $4d$; A soil could be divided into a coarse fraction ($c$) and a fines fraction ($f$). $D_{15c}$= the grain size finer

than which 15% of the coarse fraction is retained; $d_{85f}$ = the grain size finer than which 85% of the fines fraction is retained; $h_1=d_{90}/d_{60}$; $h_2=d_{90}/d_{15}$; "U" denotes unstable; "S" denotes stable.

### *2.3 Test procedures*

The initial stage of the experiment involves specimen preparation. To facilitate the tracking of particle movement, sand particles at different depths were dyed with four different stains (e.g., green, yellow, blue, and red as shown in Fig. 3). Each specimen had four layers each with a thickness of 80 mm. Each layer was prepared following the layer compaction method (LCM) with a relative density of 90%. The total height of the specimen was 320 mm. The bottom of the specimen was filled with gravels of 20 mm height. A filter mesh with a pore size of about 0.01 mm was installed between the gravel and the specimen. The gravel and the filter mesh formed a buffer zone to control the uniform flow of external water into the specimen and to reduce the impact of water flow. A wire mesh with holes of 5 mm diameter was set on the top of specimen. Another gravel layer with 20 mm height was added on top of the wire mesh. This top gravel layer provided a natural transport channel for the loss of fine particles. Also, it transferred the external load uniformly to the surface of specimen, avoiding the direct action of the loading plate.

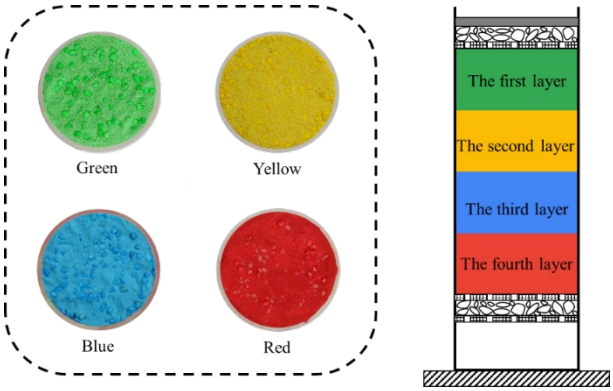


Fig.3. Dyeing of the sandy soil for different layers

The second step involves saturating the specimen. Distilled water was injected into the bottom of specimen from the water supply tank via a pipe. A buffer tank was set up to provide a steady flow of water. The water supply tank was lifted to raise the water level within the specimen until it reached the top of the container. The rate of water level rise was carefully controlled at approximately 2.0 mm/min to prevent any seepage-induced deformation. This controlled process ensured that the specimen was fully saturated with water.

The final step is starting the experiment. During this stage, the water supply tank was gradually lifted. The increase of hydraulic head in water tank can cause an augmented average hydraulic gradient, which provides increasing seepage force that drives fine particles migrate from the bottom to the top of specimen. The average hydraulic gradient is defined as follows.

$$i_a = \frac{h_1 - h_2}{l} \tag{1}$$

where $h_1$ is the height of water level in the water tank; $h_2$ is the height of the top boundary of specimen; $l$ is the thickness of specimen (i.e., 320 mm).

Fig. 4 demonstrates the average hydraulic gradient applied during the test. The significance of the critical hydraulic gradient in evaluating the stability of the test specimen is paramount. To precisely capture the critical hydraulic gradient during the internal erosion process, the gradients selection was guided by the following criteria: (1) The initiation of internal erosion in sandy soils often occurs at a low hydraulic gradient (Suits et al. 2011). To obtain an accurate hydraulic gradient at the initiation of particle loss, the external hydraulic head was controlled to increase at a low rate at the beginning of the test. (2) The hydraulic gradient leading to massive loss of fines is typically large. Therefore, the external hydraulic head was controlled to increase at a larger rate in the later stages of the test (Moffat et al. 2011). Of particular interest is the contrast between Test A-static and Test A-cyclic, where the average hydraulic gradient

applied in Test A-cyclic increases at a deliberately slower rate. This deliberate choice was made to effectively capture the intricate internal erosion behaviour under cyclic loading conditions. During this step, the mass of eroded particles and seepage velocity measured from the water collection system were continuously monitored.

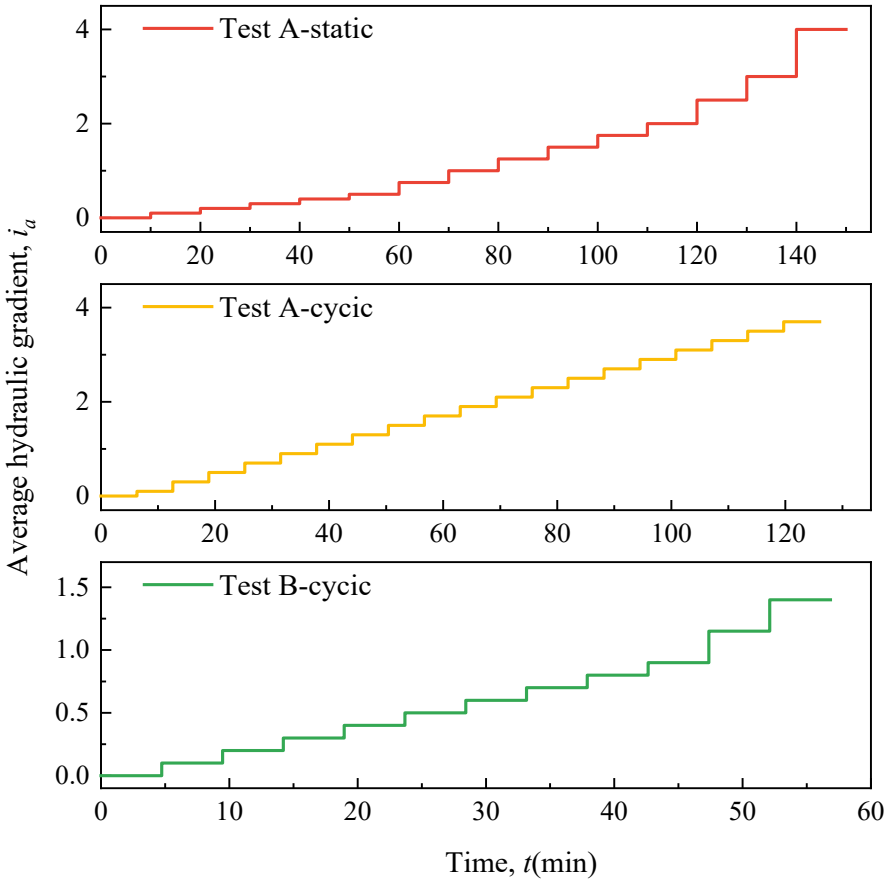


Fig.4. Average hydraulic gradient applied during the test.

## 3. Experimental results

### *3.1 Quantitative discussion of eroded particles*

3.1.1 Cumulative eroded soil mass

Fig. 5 displays the cumulative eroded soil mass obtained from the collection system. With the increase of water level in the tank, fine particles begin to erode once the average hydraulic gradient exceeds a critical value. The initiation hydraulic gradient ($i_{start}$) is defined as the

hydraulic gradient at the onset of internal erosion. For example, in Test A-static, when the average hydraulic gradient is small ($i_a$ < 2.0), fine particles remain stable and do not migrate away from skeletal particles. However, once the average hydraulic gradient increases to 2.0, a small quantity of fine particles are eroded. When the average hydraulic gradient increases from 2.0 to 4, no significant increasing in eroded particles is detected (cumulative erosion mass = 2.2 g). Overall, these findings indicate that the specimen with PSD A was tested as stable under static loading, which is consistent with the results evaluated using the currently available internal stability criterion (as shown in Table 2).

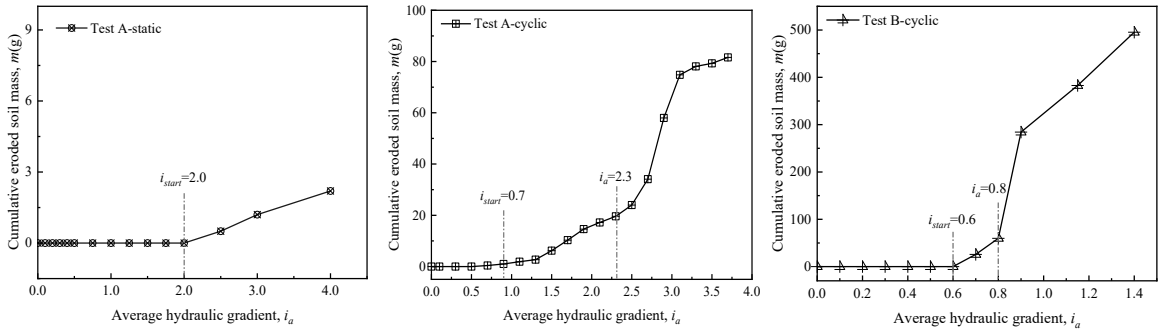


Fig.5 Cumulative eroded soil during tests

As presented in Fig. 5(b), the $i_{start}$ of Test A-cyclic is 0.7, which is only one-third of that of Test A-static. As the average hydraulic gradient grows from 0.7 to 1.7, more fine particles lose their stability, resulting in a gradual increase in the erosion rate. After this, the specimen reaches a new equilibrium state with a decreased rate of particle loss (i.e., $i_a$ = 1.7 ~ 2.3). The equilibrium state is then disrupted by the coupling effect of cyclic loading and an increased average hydraulic gradient. An approximately three-fold increase in the erosion rate is noted when the average hydraulic gradient is raised to another critical point ($i_a$ = 2.3). Eventually, the cumulative erosion mass of Test A-cyclic increases to approximately 40 times that of Test A-static. Comparing the results of the two tests with the same sand grading, it is clear that the same specimen that was stable under static loading experiences a significant loss of particles

under cyclic loading, with a final volume loss of 1.25%. These results suggest that cyclic loading has a considerable impact on the stability of the soil.

The evolution of cumulative eroded particle mass for Test B-cyclic is illustrated in Fig. 5(c). Fine particle loss initiates when the average hydraulic gradient reaches 0.6. As the average hydraulic gradient increases to 0.8, the rate of particle loss increases significantly. Then the rate decreases slightly after the average hydraulic gradient reaches 0.9. The specimen eventually experiences a significant particle loss of 4.79%. Remarkably, the critical hydraulic gradient for significant erosion observed in Test B-cyclic is one-third of that observed in Test A-cyclic, and the final cumulative eroded mass of Test B-cyclic is five times that of Test A-cyclic. These results confirm that specimen with PSD B is less stable than specimen with PSD A under cyclic loading, which is consistent with the outcomes assessed using internal stability criteria.

3.1.2 Particle-size distribution of eroded particles

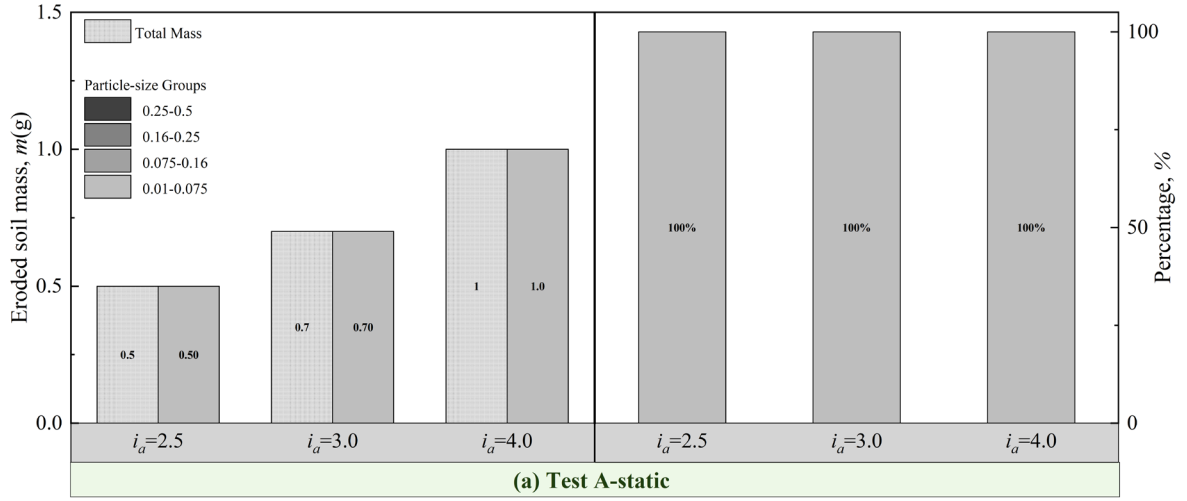

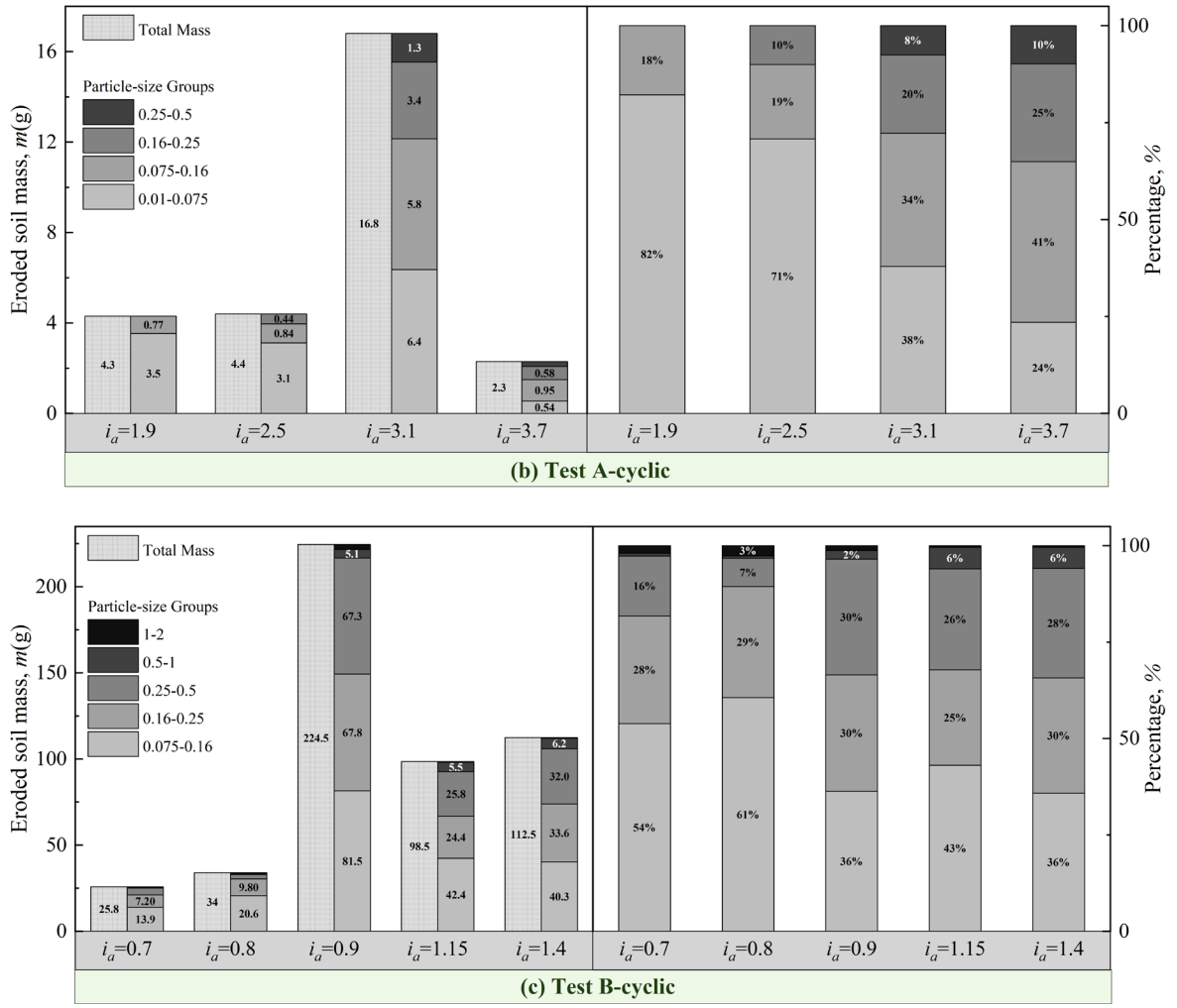


Fig.6 Size distribution of eroded particles

The particle-size distribution of eroded particles at various average hydraulic gradients can be obtained through sieving. As shown in Fig. 6(a), for Test A-static, the size of eroded particles is consistently between 0.01 mm and 0.075 mm for average hydraulic gradient from 2.5 to 4. However, there are notable differences when the same specimen is subjected to cyclic loading, as shown in Fig. 6(b). At an average hydraulic gradient of 1.9, 82% of the eroded particles have a size between 0.01 mm and 0.075 mm, and the maximum particle size is between 0.075mm and 0.16 mm. As the average hydraulic gradient increases, both the maximum size of eroded particles and the proportion of large particles increase gradually. These observations agree with the expected development pattern of internal erosion. Overall, cyclic loading not only triggers

particle loss at a smaller $i_{start}$ compared to Test A-static, but also causes the loss of larger particles.

Fig. 6(c) presents the size distribution of eroded particles in Test B-cyclic. As shown in Fig. 5, the loss of particles in Test B-cyclic develops rapidly during the test, so even a small average hydraulic gradient ($i_a$ = 0.7) can result in the loss of a small percentage of large size particles (18% between 0.25 mm and 2 mm). The evolution of eroded particles size in Test B-cyclic can be divided into two stages: (1) when the average hydraulic gradient is less than 0.8, eroded particle sizes mainly fall between 0.075 and 0.25 mm; (2) when the average hydraulic gradient exceeds 0.8, a large amount of particles are lost, and the size of eroded particles is mainly between 0.075 and 0.5 mm, with an increase in the average particle size compared to the first stage. Similar to Test A-cycle, the mass of lost particles does not increase steadily but decreases following significant erosion. This decrease is attributed to the formation of a stable structure after the loss of unstable fine particles.

### 3.1.3 Origin of eroded particles

The particle size distribution of eroded particles under a variety of hydraulic gradients is discussed in the previous paragraphs. In this section, the origin of eroded particles will be tracked based on staining technique in order to investigate which soil layer the eroded particles originate from, as well as to determine the mass proportion of eroded particles from each soil layer. The soil particles were dyed with four different colors, as shown in Fig. 3. Considering that the eroded particles are small in volume and large in quantity, which makes manual sorting difficult, a method of image recognition is applied. The Particles and Cracks Analysis System (PCAS) is employed for color identification (Liu et al. 2011, 2013). This system involves counting the area of particles with different colors in the image after binarization. In Fig. 7, the

mass ratio of particles with different colors in each single-sized particle group is determined by calculating the area ratio of the corresponding binarized image. Then the mass of each color particle can be calculated by multiplying the total mass by the mass ratio, which enables us to track the mass of particles lost from each layer. During the experiments, the particles that passed through the sieve were captured using a high-resolution digital camera with 48 megapixels. The camera maintained a consistent distance of 30 cm for each photo, resulting in an approximate actual area of 60,000 $mm^3$. According to our previous study (Zhang et al. 2022), in conjunction with the camera's pixel resolution, the image recognition technology employed can accurately identify particles as small as 0.00125 mm, ensuring high accuracy of the test.

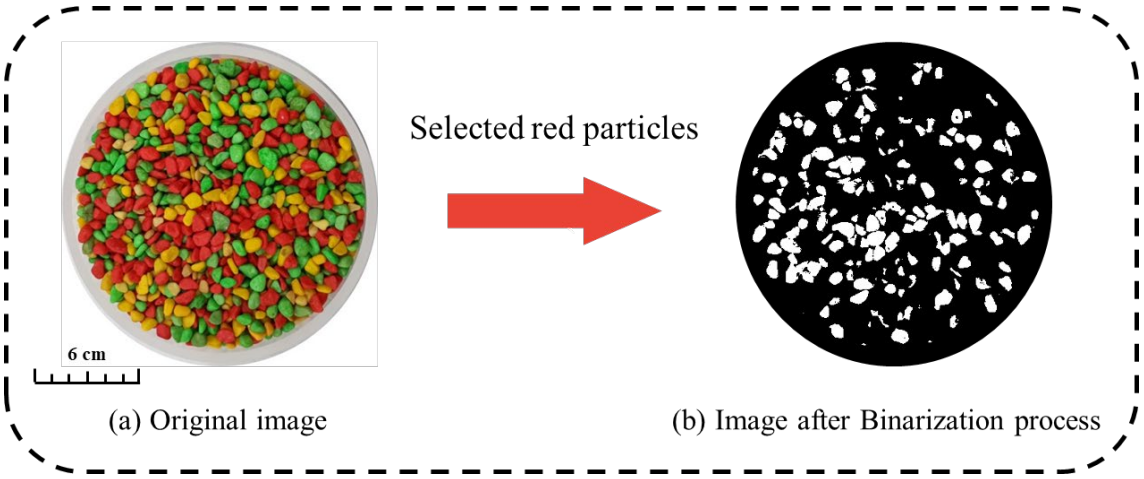


Fig.7 Image processing by Particles and Cracks Analysis System (PCAS)

Fig. 8(a) shows the origins of eroded particles for Test A-static. From an average hydraulic gradient of 2.0 to 4.0, only soil particles with the size of 0.01-0.075 mm from the first layer (green sand) are lost. For Test A-cyclic (Fig. 8(b)), during the initial stage of particle loss ($i_a$ < 2.5), only soil particles from the first layer (green sand) are lost, primarily in the size range of 0.01 mm to 0.075 mm. As the average hydraulic gradient increases to 3.1, particles with a grain size of 0.01-0.075 mm from the second layer (yellow sand) are lost, followed by the loss of particles with larger particle-size groups (0.075-0.16 mm). Fine particles from the third and

fourth layers for Test A-cyclic are not lost in the range of hydraulic gradients imposed in this study. Overall, as the average hydraulic gradient increases, there is an observed increase in both the maximum size of the lost particles and their depth from which they originated.

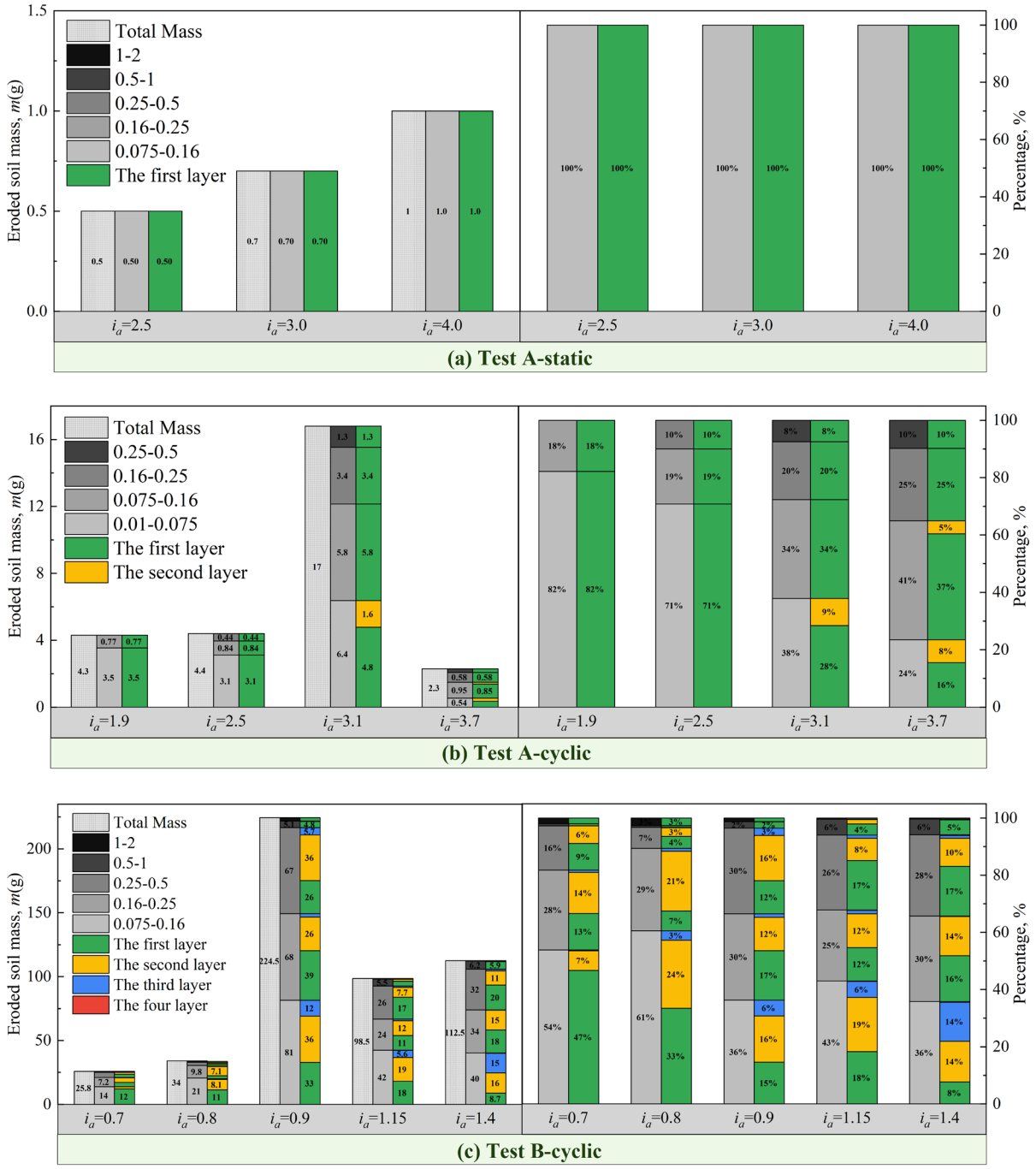


Fig.8 Origins of eroded particles

In Fig. 8(c), the origins of eroded particles during Test B-cycle are presented. At an average hydraulic gradient of 0.7, the particle loss is in the initial stage, and the eroded particles mainly consist of green (71.49%) and yellow (27.41%) sand from the first and second layers, respectively, with blue sand also present. Particles lost from the first layer are sized between 0.075-2 mm, and those lost from the second layer are sized between 0.075-1 mm. When the average hydraulic gradient increases to 0.9, significant particle loss occurs. The lost particles mainly consist of green (46.89%), yellow (43.74%), and blue (9.37%) sand, with no red particles present. Compared to the initial stage of the experiment, the overall percentage of particles lost from the second- and third-layer increase. As the average hydraulic gradient continues to rise, the mass of lost particles decreases, and a small proportion of red particles (0.26% at $i_a$ = 1.15 and 0.92% at $i_a$ = 1.4) appear, indicating that particles in the fourth layer have been eroded.

Collection systems can be utilized to obtain the total mass of eroded particles, and sieve testing can determine their particle-size distribution. In this study, we go a step further by utilizing staining and image recognition techniques to quantitatively identify the origin of eroded particles. It is critical in gaining insight into internal erosion and in preventing and mitigating potential damage, as this aspect has received limited attention in previous research. Our study's findings provide valuable contributions to the field and highlight the importance of further research in this area. During the experiment, the hydraulic gradient imposed on Test A-static caused only minor particle loss in the first layer. However, particle erosion in Test A-cyclic and B-cyclic progressed gradually from the top to the bottom, and the size of the particles lost in each layer exhibited an increasing trend with the rising hydraulic gradient.

### *3.2 Hydraulic responses*

The continuous monitoring of pore water pressure curves during internal erosion, as shown in Fig. 9, can provide valuable insights into the behavior of the tested specimens. Fig. 9(a) illustrates that pore water pressure of Test A-static increases in a stepwise manner as average hydraulic gradient increases. During each hydraulic gradient application period, the pore water pressure remains essentially constant with minor fluctuations. For Test A-cyclic (Fig. 9(b)), the initial applied hydraulic gradient is relatively small, and the pore water pressure is relatively stable with fluctuations within a certain range. At this stage, the internal structure of specimen is stable, and the hydraulic gradient is not strong enough to cause particle migration. However, as the applied average hydraulic gradient increases, the pore water pressure becomes increasingly disordered and the variation is with higher frequency and magnitude, indicating that some particles become unstable and lost. As illustrated in Fig. 9(c), Test B-cyclic shows local instability with significant fluctuations in pore water pressure. This behavior can be attributed to the significant loss of fine particles, which leads to an increase in soil porosity and a corresponding change in the response of pore water pressure to the cyclic loading.

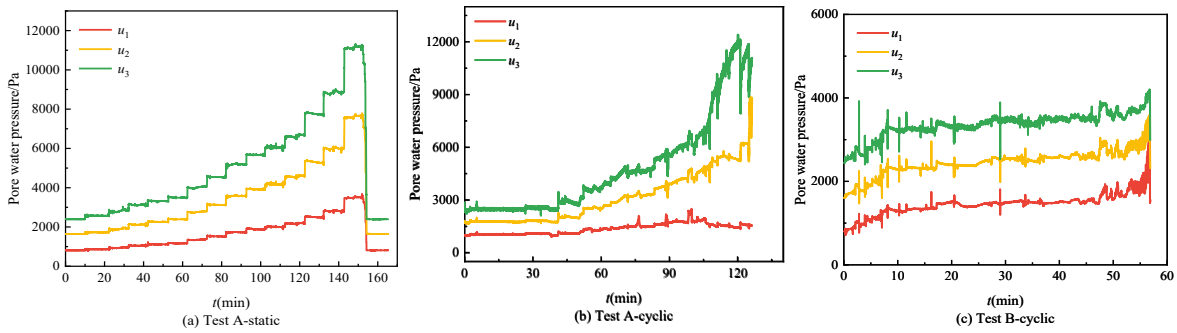


Fig.9 Time curve of pore water pressure for each specimen

The local hydraulic gradient within the specimen is a key factor to drive particle migration. In order to measure the local hydraulic gradient between different layers, we have followed

established practices by referencing current studies (Israr et al. 2016; Moffat et al. 2011; Moffat and Fannin 2011; Sufian et al. 2022). In the process, the measured pore water pressure is converted into pressure head, i.e., pressure head $H=u/\gamma_w$ (Israr and Indraratna 2018; Ueng et al. 2017). When the pore water pressures at the locations of P-1, P-2, and P-3 are different, the local hydraulic gradient $i$ in each zone is defined as:

$$i_{ij} = \frac{H_{pi}+Z_i-(H_{pj}+Z_j)}{L} \quad (2)$$

where:

$i_{ij}$ = the local hydraulic gradient between zone P-$i$ and P-$j$, and

$H_{pi}$, $H_{pj}$= the pressure head at pressure senior P-$i$ and P-$j$, and

$Z_i$, $Z_j$= the elevation head at presure senior P-$i$ and P-$j$, and

$L$= the thickness between the P-$i$ and P-$j$.

The hydraulic gradient $i_{ij}$ between the layers can be calculated by equation (2), and the results are presented in Fig. 10. As depicted in Fig. 10(a), the local hydraulic gradient of Test A-static gradually increases with the average hydraulic gradient. When the average hydraulic gradient is small, the local hydraulic gradient remains constant without fluctuation, consistent with the results obtained in Fig. 5(a), where Test A-static is stable, and no particle loss occurs. However, when the average hydraulic gradient is significant, a small amount of particle lost, and the local hydraulic gradient has a slight fluctuation. This phenomenon of fluctuation caused by particle migration is also observed experimentally by Moffat et al. (2011).

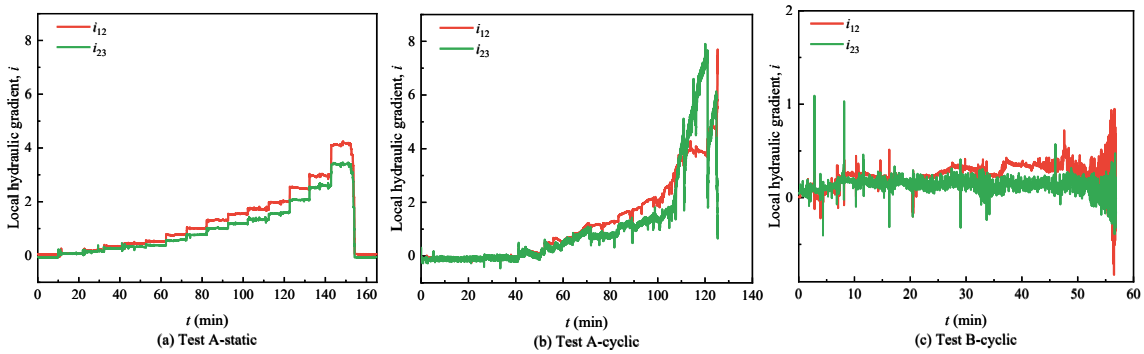

Fig.10 Time evolution of local hydraulic gradient

At the beginning of the experiment for Test A-cyclic, the stability of the specimen structure ensures that the local hydraulic gradient formed is not sufficient to drive a large amount of particle migration. As a result, the local hydraulic gradient is relatively smooth, and sudden transient changes are unlikely to occur. However, as the applied average hydraulic gradient increases, more sudden variations occur, indicating that a certain degree of particle migration has occurred. During the experiment, Test A-cyclic exhibits a maximum local hydraulic gradient of approximately 8 (at an applied average hydraulic gradient of 3.3), while Test A-static reaches about 4 (at an applied average hydraulic gradient of 4). Comparing the two specimens with the same grade, it becomes evident that local hydraulic gradient formed under cyclic loading is higher than that formed under static loading conditions. This difference can contribute to the varying degrees of particle loss observed in the specimens with the same PSD.

In Test B-cyclic, more transient and sudden variations in local hydraulic gradient are observed at the early stage, which may be attributed to local instability within the soil structure. These variations indicate that small-scale particle migration has occurred at the early stage. As the average hydraulic gradient increases and cyclic loading continues, fine particles are continuously lost from the specimen, and accordingly, the oscillation amplitude of local hydraulic gradient between layers increases. Further, this increase in turn leads to the loss of particles, and eventually to destruction of the specimen.

### *3.3 Variations in average flow velocity and porosity*

Fig.11(a) illustrates the correlation between the average flow velocity and the applied average hydraulic gradient for Test A-static. This relationship can typically be classified into two stages:

the steady seepage stage and the particle loss stage. As expected, the average flow velocity in the steady seepage stage exhibits a clear linear increase with the average hydraulic gradient. Moreover, the soil structure is relatively stable during this stage, and no particle loss occurs. These findings are further supported by the particle loss results presented in Fig. 5. Once the critical hydraulic gradient for particle erosion initiation ($i_{start}$) is reached, the slope of the curve starts to exhibit inflections, which correspond to the dancing-like behavior exhibited by the fine particles. Test A-static has a low particle loss and a light curve slope variation due to its structural stability. Notably, the average flow velocity of Test A-cyclic is more complicated during the particle loss stage. The average flow velocity increases approximately linearly with average hydraulic gradient at a greater rate after reaching the critical hydraulic gradient ($i_{start} >$ 0.7). After a period of continuous particle loss, the average flow velocity decreases briefly and the rate of particle loss slows down (as shown in Fig. 5), corresponding to a brief equilibrium state within the specimen. Once the average hydraulic gradient reaches another critical value ($i_a = 2.3$), the equilibrium state is broken, resulting in an increase in particle loss, and thus, an increase in the average flow velocity of Test A-cyclic. When the loss of unstable particles reaches a certain degree, the specimen may reach a new equilibrium state where the average flow velocity tends to be stable, and the rate of particle loss slows down. Recent studies (Fleshman and Rice 2013; Indraratna et al., 2015) have suggested that the equilibrium state of a specimen is correlated with the local and global movements of fine particles, and the corresponding critical hydraulic gradients have been explored profoundly. Fig.11(a) shows that due to the internal instability, Test B-cyclic exhibits a continuous increase in average flow velocity with the applied average hydraulic gradient during the particle loss stage, and eventually reaching a relatively stable equilibrium state.

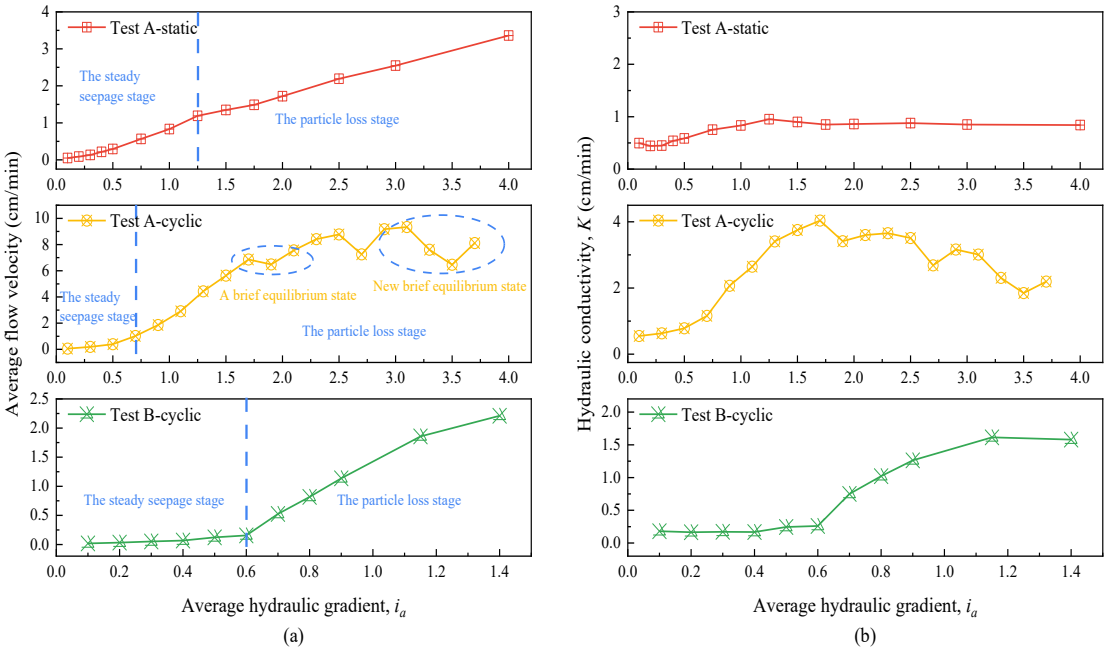


Fig.11 Variation of average flow velocity and hydraulic conductivity.

Furthermore, changes in hydraulic conductivity resulting from particle loss are determined using the average hydraulic gradient and the assumption that seepage follows Darcy's law (Ke and Takahashi 2014a). This assumption is reasonable as maximum Reynolds numbers during testing were less than 5. Fig.11(b) demonstrates that all tests exhibit a slight increase in the hydraulic conductivity before the initiation of internal erosion. This phenomenon was also observed by Ke and Takahashi (2012), which is interpreted as a characteristic feature of the upward seepage flow test. The upward seepage induces a reduction in effective stress, analogous to unloading the soil, resulting in an increase in hydraulic conductivity even in the absence of particle loss. Test A-static shows a relatively constant hydraulic conductivity, while Test A-cyclic exhibits more complex variations. Upon the onset of internal erosion in Test A-cyclic, seepage flow washes out fine particles, increasing the effective porosity and consequently the hydraulic conductivity (up to five times its initial value). However, during internal erosion, eroded particles from the lower part have a long potential travel distance, which may lead to them becoming trapped and blocked in smaller pore channels, resulting in

a reduction in effective pore throat diameter and hydraulic conductivity. In Test B-cyclic, the instability of soil structure causes a significant continuous loss of particles with the increasing average hydraulic gradient, leading to a corresponding increase in hydraulic conductivity.

Fig. 12 demonstrates the evolution of porosity at different layers with time. The porosity in this study is calculated using the three-phase relationship of soils. Specifically, since the soil is saturated, the porosity can be determined as follows.

$$n = \frac{V_v}{V} = \frac{\left(V_w / S_r\right)}{V} = \frac{\theta}{S_r} \tag{3}$$

where $V_v$ is the volume of voids, $V_w$ is the volume of pore water, $V$ is the total volume, $S_r$ is the degree of saturation of the soil, and $\theta$ is the volumetric water content, which is measured by the Ec-5 humidity sensor. Recent investigations have shown that the degree of saturation during the erosion process is usually considered to be saturated (Jiang and Soga 2017, 2019; Ke and Takahashi 2014a; b). Specimens were carried out with a saturation procedure before loading and considered fully saturated ($S_r$=1) during the investigation due to the excellent permeability of cohesionless sandy soil. The porosity can be obtained by measuring the changes in volumetric water content. Notably, the calculated values of porosity, although reflecting only the properties at the sensor location, are still representative.

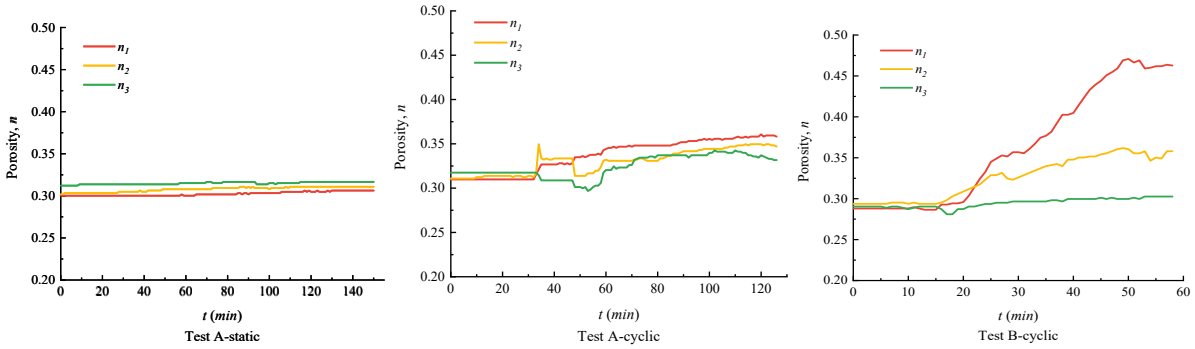


Fig.12 Local porosity of specimens at different depths

As shown in Fig.12, the porosity changes of Test A-static are small. This is attributed to Test A-static experiencing only slight particle loss, allowing the soil structure to remain largely unchanged. In Test A-cyclic, the porosity of each layer remains stable at low average hydraulic gradients, signifying that the specimen was in the steady seepage stage with relatively minor alterations in hydraulic conductivity. However, as the average hydraulic gradient increases to a critical value, the specimen transitioned into the particle loss stage, resulting in an increase in porosity and hydraulic conductivity. In addition, it is worth noting that the clogging behavior of particles during transport in porous media can result in a reduction of local porosity and a corresponding decrease in local hydraulic conductivity. Test B-cyclic demonstrated structural instability characterized by continuous particle loss, leading to a substantial increase in porosity. The considerable porosity variation in Test B-cyclic indicates significant particle loss and a notable increase in hydraulic conductivity. Specifically, porosity changes are more pronounced in the upper part of the specimen than in the lower part, indicating that the lost particles mainly originate from the upper part. These porosity changes are consistent with the results obtained from particle loss analysis. In summary, the alterations in porosity align with the hydraulic conductivity outcomes presented in Fig. 11. In the steady seepage stage, the soil structure remains unaltered, resulting in minimal fluctuations in both porosity and hydraulic conductivity. Conversely, during the particle loss stage, substantial shifts in porosity are evident, which correspondingly influence hydraulic conductivity.

## 4. Discussions

Fig. 13 shows a typical local hydraulic gradient variation curve generated during our cyclic loading test, capturing a specific point in time when cyclic loading is applied. Under static loading conditions, the specimen maintains stable seepage, with local hydraulic gradients remaining relatively constant. Conversely, the introduction of cyclic loading induces transient

vibrations within the soil, leading to interactions between soil particles and pore water. These interactions result in the generation of impulsive dynamic water pressures, ultimately causing oscillations in the local hydraulic gradients. When the average hydraulic gradient applied to the soil is low, the local hydraulic gradient formed between layers is also small, and the infiltration force is not strong enough to drive soil particles to migrate. However, the application of cyclic loading generates an oscillating hydraulic gradient that forms an oscillating infiltration force on soil particles, disturbing the fine particles and affecting the stability of soil structure. When the average hydraulic gradient is small (even below the critical hydraulic gradient for particle initiation under static load), the high hydraulic gradient generated by the transient excitation of cyclic loading may reach the initiation hydraulic gradient, causing soil particles to break away from skeleton and start migrating. This phenomenon explains why the $i_{start}$ of Test A-cyclic is much smaller than that of Test A-static. As soil particles erode, the void ratio increases, resulting in greater transient excitation under the same load. This transient reduction of pore space will generate a greater impulsive dynamic water pressure. With continuous erosion of particles, the transient excitation caused by cyclic loading gradually intensifies, leading to further particle loss.

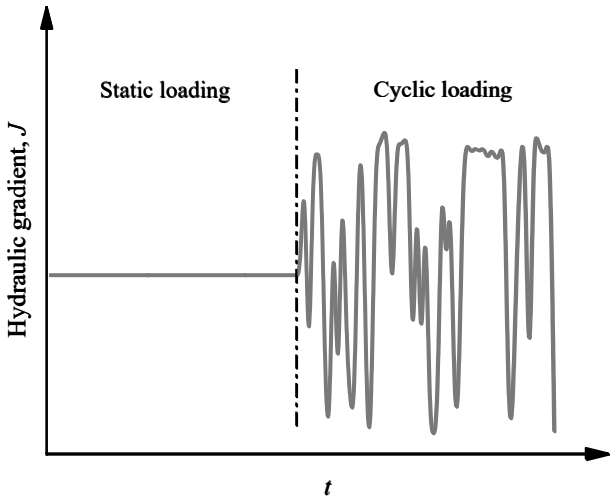


Fig.13 Changes of hydraulic gradient before and after cyclic load

This study set out with the aim of assessing the impacts of cyclic loading on internal stability, comparing the internal erosion patterns of Tests A-static, A-cyclic, and B-cyclic. The main findings are as follows:

(1) Critical hydraulic gradient: The critical value $i_{start}$ for the initiation of particle loss in Test A-static is about three times that of Test A-cyclic. The critical hydraulic gradient for significant particle loss in Test A-cyclic is three times that in Test B-cyclic.

(2) Mass loss: Test A-cyclic has a final mass loss about 40 times that of Test A-static. The total final mass loss of Test B-cyclic is six times greater than that of Test A-cyclic.

(3) Local hydraulic gradient: Cyclic loading generates a higher local hydraulic gradient in the specimen than static loading with the same average hydraulic gradient, which is the reason for the varying degrees of particle loss among specimens with the same PSD. Under cyclic loading, Test B-cyclic experiences a larger amplitude of hydraulic gradient oscillation and more abrupt changes than Test A-cyclic.

(4) Porosity and hydraulic conductivity: The porosity and hydraulic conductivity in Test A-static remain stable due to the limited particle loss occurring only in the first layer. In contrast, Test A-cyclic experiences particle loss from the first and second layers, resulting in a significant change in porosity and hydraulic conductivity compared to Test A-static. Test B-cyclic exhibits particle loss from even deeper layers, and the massive particle loss leads to a significant change in porosity and corresponding hydraulic conductivity.

One interesting finding is that, based on existing criteria discussed before, Tests A-static and A-cyclic with the same PSD are characterized as internally stable. However, the data reported here show that specimen A-cyclic is instable with the effect of cyclic loading. Previous studies have also noted the importance of cyclic loading on the internal stability of granular filters

(Indraratna et al. 2022; Israr and Israr 2017). Based on our present study, we have identified two potential causes for the observed differences between the specimens. Firstly, with the same average hydraulic gradient applied to the specimen, cyclic loading can, at certain moments, create a larger local hydraulic gradient in comparison to static loading, and thus particles are more likely to reach the critical state of erosion under cyclic loading. Secondly, the oscillating local hydraulic gradient formed between specimen layers under cyclic loading gives rise to oscillatory seepage forces. These forces have the potential to accelerates the destruction of soil spatial structure and heighten the probability of particle detachment. It should be noted that Test A-cyclic is internally more stable than Test B-cyclic. These results are in line with previous studies and provide further support for the accuracy of existing criteria in evaluating the relative capability of specimens against internal stability. Notwithstanding the relatively limited tests, this work offers valuable insights into the impacts of cyclic loading on internal erosion. A further study with more focus on the effects of cyclic loading characteristics such as loading frequency, magnitude, and loading form is therefore suggested.

## 5. Conclusions

In this study, the impact of cyclic loading on the internal erosion of sandy soils was examined through tests conducted on three saturated granular soils using a specially designed hydraulic apparatus. The main conclusions are summarized as follows.

The internal erosion under cyclic loading is more intricate and distinct from that under static loading conditions. The development of oscillating hydraulic gradients due to cyclic loading leads to internal instability and triggers excessive erosion of fines from specimens. For example, the results show that internally stable samples have an $i_{start}$ of 2.0 and a final cumulative erosion

fine of no more than 5 g in static loading, however, under cyclic loading, $i_{start}$ is 0.7 and the final cumulative erosion fines even exceeds 80 g.

Based on particle staining and image recognition techniques, the composition and origin of lost particles are quantitatively described. Fine particles are mainly lost initially, and a new equilibrium state will be reached after a certain mass of particle loss occurs. Particle erosion develops from the top to the bottom, and the maximum size of eroded particles from each layer gradually increases.

Existing criteria based on the geometric properties of soil are still reliable in assessing internal stability. However, when subjected to cyclic loading, oscillating local hydraulic gradients are formed between different layers, which presents a challenge to the internal stability of specimen. Incorporation of cyclic loading conditions into these criteria is a more realistic way to evaluate the internal erosion stability of soils, especially in the design of structures with external disturbances, such as high-speed rail substructures.

## ACKNOWLEDGEMENTS

This research was supported by the Australian Research Council (https://www.arc.gov.au/) Discovery Early Career Researcher Award (DECRA; DE220100763), Young Scientists Fund of the National Natural Science Foundation of China (No. 52308438), the Fellowship of China National Postdoctoral Program for Innovative Talents (No. BX20220259), the Open Fund of Hunan International Scientific and Technological Innovation Cooperation Base of Advanced Construction and Maintenance Technology of Highway (No. kfj220801) and the Changsha Natural Science Foundation (No. kq2208234).

## Competing Interest Statement

There are no competing interests in this paper.

## Data Availability Statement

Some or all data, models or code generated or used during the study are available from the corresponding author by request.

## REFERENCE


ASTM. 2014. C136/C136M: Standard Test Method for Sieve Analysis of Fine and Coarse Aggregates. ASTM International, West Conshohocken, PA, USA.

Bonelli, S., O. Brivois, R. Borghi, and N. Benahmed. 2006. On the modelling of piping erosion. *Comptes Rendus Mécanique*, 334 (8–9): 555–559. https://doi.org/10.1016/j.crme.2006.07.003.

Burenkova, V. V. 1993. *Assessment of suffusion in non-cohesive and graded soils. filters in geotechnical and hydraulic engineering.* The Netherlands：Rotterdam.

Chang, D. S., and L. M. Zhang. 2013. Extended internal stability criteria for soils under seepage. *Soils and Foundations*, 53 (4): 569–583. https://doi.org/10.1016/j.sandf.2013.06.008.

Che, H., C. O'Sullivan, A. Sufian, and E. R. Smith. 2021. A novel CFD-DEM coarse-graining method based on the Voronoi tessellation. *Powder Technology*, 384: 479–493. https://doi.org/10.1016/j.powtec.2021.02.025.

Crosta, G., and C. di Prisco. 1999. On slope instability induced by seepage erosion. *Can. Geotech. J.*, 36 (6): 1056–1073. https://doi.org/10.1139/t99-062.

David Suits, L., T. Sheahan, R. Moffat, and R. Fannin. 2006. A Large Permeameter for Study of Internal Stability in Cohesionless Soils. *Geotech. Test. J.*, 29 (4): 100021. https://doi.org/10.1520/GTJ100021.

Fell, R., C. F. Wan, J. Cyganiewicz, and M. Foster. 2003. Time for Development of Internal Erosion and Piping in Embankment Dams. *J. Geotech. Geoenviron. Eng.*, 129 (4): 307–314. https://doi.org/10.1061/(ASCE)1090-0241(2003)129:4(307).

Fleshman, M. S., and J. D. Rice. 2013. Constant Gradient Piping Test Apparatus for Evaluation of Critical Hydraulic Conditions for the Initiation of Piping. *Geotech. Test. J.*, 36 (6): 20130066. https://doi.org/10.1520/GTJ20130066.

Fleshman, M. S., and J. D. Rice. 2014. Laboratory Modeling of the Mechanisms of Piping Erosion Initiation. *J. Geotech. Geoenviron. Eng.*, 140 (6): 04014017. https://doi.org/10.1061/(ASCE)GT.1943-5606.0001106.

Flores-Berrones, R., M. Ramírez-Reynaga, and E. J. Macari. 2011. Internal Erosion and Rehabilitation of an Earth-Rock Dam. *J. Geotech. Geoenviron. Eng.*, 137 (2): 150–160. https://doi.org/10.1061/(ASCE)GT.1943-5606.0000371.

Foster, M., Fell, R., and Spannagle, M. (2000). The statistics of embankment dam failures and accidents. *Canadian Geotechnical Journal*, 37(5), 1000-1024.

Gao, F., S. Zhang, X. He, and D. Sheng. 2022. Experimental Study on Migration Behavior of Sandy Silt under Cyclic Load. *J. Geotech. Geoenviron. Eng.*, 148 (5): 06022003. https://doi.org/10.1061/(ASCE)GT.1943-5606.0002796.

Gollin, D., W. Brevis, E. T. Bowman, and P. Shepley. 2017. Performance of PIV and PTV for granular flow measurements. *Granular Matter*, 19 (3): 42. https://doi.org/10.1007/s10035-017-0730-9.

He, X., H. Xu, W. Li, and D. Sheng. 2020. An improved VOF-DEM model for soil-water interaction with particle size scaling. *Computers and Geotechnics*, 128: 103818. https://doi.org/10.1016/j.compgeo.2020.103818.

Hunter, R. P., and E. T. Bowman. 2018. Visualisation of seepage-induced suffusion and suffosion within internally erodible granular media. *Géotechnique*, 68 (10): 918–930. https://doi.org/10.1680/jgeot.17.P.161.

Indraratna, B., J. Israr, and C. Rujikiatkamjorn. 2015. Geometrical Method for Evaluating the Internal Instability of Granular Filters Based on Constriction Size Distribution. *J. Geotech. Geoenviron. Eng.*, 141 (10): 04015045. https://doi.org/10.1061/(ASCE)GT.1943-5606.0001343.

Indraratna, B., M. Singh, T. T. Nguyen, C. Rujikiatkamjorn, R. S. Malisetty, J. Arivalagan, and L. Nair. 2022. Internal Instability and Fluidisation of Subgrade Soil under Cyclic Loading. *Indian Geotech J*. https://doi.org/10.1007/s40098-022-00616-0.

Indraratna, B., V. T. Nguyen, and C. Rujikiatkamjorn. 2011. Assessing the Potential of Internal Erosion and Suffusion of Granular Soils. *J. Geotech. Geoenviron. Eng.*, 137 (5): 550–554. https://doi.org/10.1061/(ASCE)GT.1943-5606.0000447.

Israr, J., and B. Indraratna. 2018. Mechanical response and pore pressure generation in granular filters subjected to uniaxial cyclic loading. *Can. Geotech. J.*, 55 (12): 1756–1768. https://doi.org/10.1139/cgj-2017-0393.

Israr, J., and J. Israr. 2017. Experimental Investigation and Assessment of Internal Stability of Granular Filters under One-Dimensional Static and Cyclic Loading. *Geotech. Test. J.*, 41 (1): 20170027. https://doi.org/10.1520/GTJ20170027.

Israr, J., B. Indraratna, and C. Rujikiatkamjorn. 2016. "Laboratory Investigation of the Seepage Induced Response of Granular Soils Under Static and Cyclic Loading." *Geotech. Test. J.*, 39 (5): 20150288. https://doi.org/10.1520/GTJ20150288.

Istomina, V. S. 1957. *Filtration Stability of Soils*. Moscow: Gostroizdat.

Jiang, H., X. Bian, Y. Chen, and J. Han. 2015. "Impact of Water Level Rise on the Behaviors of Railway Track Structure and Substructure: Full-Scale Experimental Investigation." *Transportation Research Record*, 2476 (1): 15–22. https://doi.org/10.3141/2476-03.

Jiang, N.-J., and K. Soga. 2017. The applicability of microbially induced calcite precipitation (MICP) for internal erosion control in gravel–sand mixtures. *Géotechnique*, 67 (1): 42–55. https://doi.org/10.1680/jgeot.15.P.182.

Jiang, N.-J., and K. Soga. 2019. Erosional behavior of gravel-sand mixtures stabilized by microbially induced calcite precipitation (MICP). *Soils and Foundations*, 59 (3): 699–709. https://doi.org/10.1016/j.sandf.2019.02.003.

Jin, W., Z. Deng, G. Wang, D. Zhang, and L. Wei. 2022. Internal Erosion Experiments on Sandy Gravel Alluvium in an Embankment Dam Foundation Emphasizing Horizontal Seepage and High Surcharge Pressure. *Water*, 14 (20): 3285. https://doi.org/10.3390/w14203285.

Johnston, I., W. Murphy, and J. Holden. 2021. "A review of floodwater impacts on the stability of transportation embankments." *Earth-Science Reviews*, 215: 103553. https://doi.org/10.1016/j.earscirev.2021.103553.

Ke, L., and A. Takahashi. 2012. Strength reduction of cohesionless soil due to internal erosion induced by one-dimensional upward seepage flow. *Soils and Foundations*, 52 (4): 698–711. https://doi.org/10.1016/j.sandf.2012.07.010.

Ke, L., and A. Takahashi. 2014a. Triaxial Erosion Test for Evaluation of Mechanical Consequences of Internal Erosion. *Geotech. Test. J.*, 37 (2): 20130049. https://doi.org/10.1520/GTJ20130049.

Ke, L., and A. Takahashi. 2014b. Experimental investigations on suffusion characteristics and its mechanical consequences on saturated cohesionless soil. *Soils and Foundations*, 54 (4): 713–730. https://doi.org/10.1016/j.sandf.2014.06.024.

Kenney, T. C., and Lau, D. (1985). Internal stability of granular filters. *Can. Geotech. J.*, 22(2), 215-225.

Kenney, T. C., and Lau, D. (1986). Internal stability of granular filters：Reply. *Can. Geotech. J.*, 23, 420-423.

Kezdi, A. 1979. *Soil physics：selected topics*. Elsevier Science, New York, Amsterdam.

Lian, Y., H. H. Bui, G. D. Nguyen, H. T. Tran, and A. Haque. 2021. A general SPH framework for transient seepage flows through unsaturated porous media considering anisotropic diffusion. *Computer Methods in Applied Mechanics and Engineering*, 387: 114169. https://doi.org/10.1016/j.cma.2021.114169.

Liang, Y., T.-C. J. Yeh, Y. Zha, J. Wang, M. Liu, and Y. Hao. 2017. Onset of suffusion in gap-graded soils under upward seepage. *Soils and Foundations*, 57 (5): 849–860. https://doi.org/10.1016/j.sandf.2017.08.017.

Liu, C., B. Shi, J. Zhou, and C. Tang. 2011. Quantification and characterization of microporosity by image processing, geometric measurement and statistical methods: Application on SEM images of clay materials. *Applied Clay Science*, 54 (1): 97–106. https://doi.org/10.1016/j.clay.2011.07.022.

Liu, C., C.-S. Tang, B. Shi, and W.-B. Suo. 2013. Automatic quantification of crack patterns by image processing. *Computers & Geosciences*, 57: 77–80. https://doi.org/10.1016/j.cageo.2013.04.008.

Ma, G., H. H. Bui, Y. Lian, K. M. Tran, and G. D. Nguyen. 2022. A five-phase approach, SPH framework and applications for predictions of seepage-induced internal erosion and failure in unsaturated/saturated porous media. *Computer Methods in Applied Mechanics and Engineering*, 401: 115614. https://doi.org/10.1016/j.cma.2022.115614.

Ma, Q., A. Wautier, and W. Zhou. 2021. Microscopic mechanism of particle detachment in granular materials subjected to suffusion in anisotropic stress states. *Acta Geotech.*, 16 (8): 2575–2591. https://doi.org/10.1007/s11440-021-01301-x.

Maknoon, M., and T.-F. Mahdi. 2010. Experimental investigation into embankment external suffusion. *Nat Hazards*, 54 (3): 749–763. https://doi.org/10.1007/s11069-010-9501-1.

Mao, changxi. 2005. Study on piping and filters: part I of piping. *Rock and Soil Mechanics*, 2 (26): 209–215.

Moffat, R., and R. J. Fannin. 2011. "A hydromechanical relation governing internal stability of cohesionless soil." *Can. Geotech. J.*, 48 (3): 413–424. https://doi.org/10.1139/T10-070.

Moffat, R., R. J. Fannin, and S. J. Garner. 2011. Spatial and temporal progression of internal erosion in cohesionless soil. *Can. Geotech. J.*, 48 (3): 399–412. https://doi.org/10.1139/T10-071.

Moraci, N., M. C. Mandaglio, and D. Ielo. 2014. Analysis of the internal stability of granular soils using different methods. *Can. Geotech. J.*, 51 (9): 1063–1072. https://doi.org/10.1139/cgj-2014-0006.

Qu, C.-Z., Y. Wang, L. Wei, and Z. Guo. 2012. In-situ test and analysis of vibration of subgrade for Wuhan-Guangzhou high-speed railway. *Rock and Soil Mechanics*, 33(5), 1451-1461. https://doi.org/10.16285/j.rsm.2012.05.028.

Richards, K. S., and K. R. Reddy. 2007. Critical appraisal of piping phenomena in earth dams. *Bull Eng Geol Environ*, 66 (4): 381–402. https://doi.org/10.1007/s10064-007-0095-0.

Scheuermann, A., I. Vardoulakis, P. Papanastasiou, and M. Stavropoulou. 2002. A Sand Erosion Problem in Axial Flow Conditions on the Example of Contact Erosion due to Horizontal Groundwater Flow. *IUTAM Symposium on Theoretical and Numerical Methods in Continuum Mechanics of Porous Materials*, Solid Mechanics and Its Applications, W. Ehlers, ed., 169–175. Dordrecht: Kluwer Academic Publishers.

Shire, T., and C. O'Sullivan. 2013. Micromechanical assessment of an internal stability criterion. *Acta Geotech.*, 8 (1): 81–90. https://doi.org/10.1007/s11440-012-0176-5.

Sufian, A., T. Bittner, T. Bore, M. Bajodek, and A. Scheuermann. 2022. Physical observations of the transient evolution of the porosity distribution during internal erosion using spatial time domain reflectometry. *Can. Geotech. J.*, 59 (8): 1443–1458. https://doi.org/10.1139/cgj-2021-0570.

Suits, L. D., T. C. Sheahan, D. S. Chang, and L. M. Zhang. 2011. A Stress-controlled Erosion Apparatus for Studying Internal Erosion in Soils. *Geotech. Test. J.*, 34 (6): 103889. https://doi.org/10.1520/GTJ103889.

Tian, Z., T. Ren, R. Horton, and J. L. Heitman. 2020. "Estimating soil bulk density with combined commercial soil water content and thermal property sensors." *Soil and Tillage Research*, 196: 104445. https://doi.org/10.1016/j.still.2019.104445.

Tran, K. M., H. H. Bui, and G. D. Nguyen. 2022. DEM modelling of unsaturated seepage flows through porous media. *Comp. Part. Mech.*, 9 (1): 135–152. https://doi.org/10.1007/s40571-021-00398-x.

Trautz, A. C., K. M. Smits, and A. Cihan. 2015. "Continuum-scale investigation of evaporation from bare soil under different boundary and initial conditions: An evaluation of nonequilibrium phase change: NONEQUILIBRIUM PHASE CHANGE IN POROUS MEDIA." *Water Resour. Res.*, 51 (9): 7630–7648. https://doi.org/10.1002/2014WR016504.

Ueng, T.-S., Z.-F. Wang, M.-C. Chu, and L. Ge. 2017. Laboratory tests for permeability of sand during liquefaction. *Soil Dynamics and Earthquake Engineering*, 100: 249–256. https://doi.org/10.1016/j.soildyn.2017.05.037.

US Army Crops Engineering Engineers. 1953. *Filter experiments and design criteria technical memorandum No.3-360.* Vicksburg: Waterways Experiment Station.

Wang, G., Z. Deng, J. Yang, X. Chen, and W. Jin. 2022. A Large-Scale High-Pressure Erosion Apparatus for Studying Internal Erosion in Gravelly Soils under Horizontal Seepage Flow. *Geotech. Test. J.*, 45 (6): 20220045. https://doi.org/10.1520/GTJ20220045.

Wautier, A., S. Bonelli, and F. Nicot. 2019. DEM investigations of internal erosion: Grain transport in the light of micromechanics. *Int J Numer Anal Methods Geomech*, 43 (1): 339–352. https://doi.org/10.1002/nag.2866.

Wicki, A., P. Lehmann, C. Hauck, S. I. Seneviratne, P. Waldner, and M. Stähli. 2020. "Assessing the potential of soil moisture measurements for regional landslide early warning." *Landslides*, 17 (8): 1881–1896. https://doi.org/10.1007/s10346-020-01400-y.

Xiao, M., and N. Shwiyhat. 2012. Experimental Investigation of the Effects of Suffusion on Physical and Geomechanic Characteristics of Sandy Soils. *Geotech. Test. J.*, 35 (6): 104594. https://doi.org/10.1520/GTJ104594.

Yan, G., Z. Li, T. Bore, S. A. Galindo Torres, A. Scheuermann, and L. Li. 2022. A lattice Boltzmann exploration of two-phase displacement in 2D porous media under various pressure boundary conditions. *Journal of Rock Mechanics and Geotechnical Engineering*, 14 (6): 1782–1798. https://doi.org/10.1016/j.jrmge.2022.05.003.

Yang, J., Z.-Y. Yin, F. Laouafa, and P.-Y. Hicher. 2019. Modeling coupled erosion and filtration of fine particles in granular media. *Acta Geotech.*, 14 (6): 1615–1627. https://doi.org/10.1007/s11440-019-00808-8.

Yin, Z.-Y., J. Yang, F. Laouafa, and P.-Y. Hicher. 2020. A framework for coupled hydro-mechanical continuous modelling of gap-graded granular soils subjected to suffusion. *European Journal of Environmental and Civil Engineering*, 1–22. https://doi.org/10.1080/19648189.2020.1795724.

Zhang, P., L. Qiu, Y. Chen, Y. Zhao, L. Kong, A. Scheuermann, L. Li, and S. A. Galindo-Torres. 2023. Coupled metaball discrete element lattice Boltzmann method for fluid-particle systems with non-spherical particle shapes: A sharp interface coupling scheme. *Journal of Computational Physics*, 479: 112005. https://doi.org/10.1016/j.jcp.2023.112005.

Zhang, S., F. Gao, X. He, Q. Chen, and D. Sheng. 2021. Experimental study of particle migration under cyclic loading: effects of load frequency and load magnitude. *Acta Geotech.*, 16 (2): 367–380. https://doi.org/10.1007/s11440-020-01137-x.

Zhang, S., J.-L. Wang, and C.-X. Tong. 2022. A breakage matrix methodology to predict particle size evolution of calcareous sands. *Powder Technology*, 407: 117626. https://doi.org/10.1016/j.powtec.2022.117626.